ADVANCED MATERIALS
www.advmat.de

A Facile and Rational Method to Tailor the Symmetry of Au@Ag Nanoparticles

Bing Ni, Jian Zhou, Levin Stolz, and Helmut Cölfen**

Precisely controlling the morphologies of plasmonic metal nanoparticles (NPs) is of great importance for many applications. Here, a facile seed-mediated growth method is demonstrated that tailors the morphologies of Au@Ag NPs from cubes/cuboids to chiral truncated cuboids/octahedra, well-defined octahedra, and tetrahedra, via simply increasing the concentrations of $AgNO_3$ and cysteine in the halide surfactant systems. Accordingly, the particle symmetries are also tuned. The method is quite robust where seeds with distinct shapes including irregular ones can all lead to uniform Au@Ag NPs. The evolution of these shapes can be illustrated by a recently proposed symmetry-based kinematic theory (SBKT). Furthermore, SBKT shows a strategy to optimize the preparation of chiral/dissymmetric NPs, and the experimental results confirm such a dissymmetric synthesis strategy. Cuboids and octahedra with corners differently truncated are identified as two different chiral forms. The chirality of the NPs is additionally probed by electrochemistry, where the chiral NPs show enantioselectivity in the oxidation of D- and L-glucose. Altogether, the results gain fundamental insights into tailoring the plasmonic NP morphologies, and also suggest strategies to obtain chiral NPs.

1. Introduction

Ag nanoparticles (NPs) have been intensively explored toward a broad range of applications, such as localized surface plasmon resonance (LSPR), electronics, sensing, biomedicine, and catalysis.[1–4] Ag almost has the strongest LSPR effects across the spectrum from 300 to 1200 nm compared with other metals, making it the probably most important material in plasmonics.[5] Furthermore, Ag is a key catalytic material for many industrial processes,[6] especially the production of ethylene oxide by ethylene epoxidation.[7] Ethylene oxide, which is produced annually on a scale of ≈25 million tons in 2021, is an important platform compound toward many different end-user industries such as automotive, agrochemicals, food and beverage, and textile.[6,7] Most of these applications are strongly dependent on the surface features of the particles. Therefore, the shape control of Ag NPs has attracted wide attention. Over the past decades, a wealth of methods has been developed for the fabrication of different Ag shapes. The polyol process is probably the most widely used approach among them. Single-crystalline spheres, cubes, octahedra, bars, spheroids, etc., and particles with planar defects such as bipyramids and penta-twinned rods, could all be prepared via the polyol processes by varying the type of polyols, precursor types, surfactants, reaction temperatures, concentrations, or introduction of trace ions.[5,6,8] However, the process is typically conducted at high temperatures (140–160 °C), and the use of organic solvents also makes it environmentally less friendly. In addition, the polyol process is usually very sensitive to impurities (such as trace amounts of halides, Fe^{2+}/Fe^{3+}, and dissolved O_2), as well as water content, which makes the synthesis sometimes difficult to replicate.[9] Some other methods like light-mediated growth and seed-mediated growth are also used to prepare different shapes. The light-mediated growth could be adopted to prepare nanoprisms with twin defects and penta-twined rods.[10,11] There is also one report on using light to guide the growth of Ag tetrahedra.[12] Many of the discussed processes also rely on the usage of seeds, and hence can be categorized into seed-mediated growth as well. The seed-mediated growth generally offers better control of the shapes due to the temporarily separated nucleation and growth stages.[13]

Since the small-sized Ag seeds are normally easy to deteriorate during storage, Au NPs are also used to prepare Au@Ag NPs via a seed-mediated growth process. After all, the plasmonic and catalytic properties of the NPs mostly depend on the exposed surfaces and shapes, that is, the Ag shell. Halide surfactants systems have been adopted to prepare particles enclosed by {100} facets, such as Au@Ag cubes and cuboids.[14,15] However, the shape diversity in these systems is highly limited. Regarding the exploration to tune the Au@Ag morphologies, there are several attempts to prepare

B. Ni, J. Zhou, H. Cölfen
Physical Chemistry
University of Konstanz
Universitätsstrasse 10, 78457 Konstanz, Germany
E-mail: bing.ni@uni-konstanz.de; helmut.coelfen@uni-konstanz.de
L. Stolz
Department of Physics
University of Konstanz
Universitätsstrasse 10, 78457 Konstanz, Germany
The ORCID identification number(s) for the author(s) of this article can be found under https://doi.org/10.1002/adma.202209810.

DOI: 10.1002/adma.202209810

Au@Ag chiral NPs,[16,17] inspired by the impressive progress on the chiral Au NPs.[18–21] Nonetheless, the chiral shapes have not been well illustrated and the measured optical activities remained at the level of chiral small molecules. Plasmonic chirality has been a hot topic recently,[22] and different chiral forms of Au NPs including clusters, discrete helical NPs, and assembling structures, have been found, and subjected to different applications, respectively.[20,23,24] On the contrary, the chiral forms of Ag or Au@Ag are scarce.[23] Many of the dissymmetric systems rely on the assembling of small NPs with the help of chiral matrixes.[25–28] The research on the chiral NP shapes has been lagging, although some reports already demonstrated the potential of using chiral Ag NPs to deliver enantioselectivity toward molecular asymmetric catalysis, even though the NPs are not clearly confirmed to be chiral.[29,30] Due to the theoretically strong plasmonic effects and the versatile catalytic performance of Ag, it would be highly rewarding to explore the chirality of Ag or Au@Ag NPs.

Here we demonstrate a simple and robust system to facilely tailor the morphology of Au@Ag NPs. The shapes could be readily tuned from cuboids/cubes to chiral truncated cuboids/octahedra, well-defined octahedra, and (truncated) tetrahedra via simply increasing the concentrations of $AgNO_3$ precursor and cysteine in the halide surfactant systems. Accordingly, the symmetries of the particles are changed in the range of $4/mmm$ (cuboids), $\frac{4}{m}\bar{3}\frac{2}{m}$ (cubes, octahedra), $\bar{4}3m$ (tetrahedra), and asymmetry (chiral truncated cuboids/octahedra) (Figure S1, Supporting Information). These morphology transitions could be explained by a recently proposed symmetry-based kinematic theory (SBKT).[31,32] The SBKT takes advantage of the basic growth processes (the surface nucleation process and the layer advancement process), and uses the preferential growth directions (PGDs) and the properties of the kinematic waves (propagation, dissipation, and interaction) to correlate the basic growth processes at the atomic scale with the NP shape evolution at the nanoscale. In an fcc lattice system, cubes/cuboids could be evolved with PGDs of <111> directions, while octahedra and tetrahedra could be prepared with PGDs of <100> directions. The difference between octahedra and tetrahedra are the surface nucleation sites, where octahedra feature corner nucleation sites and tetrahedra feature edge nucleation sites. The function of the kinematic wave is to eliminate non-uniformities during the growth, leading to particles conforming the lattice symmetry after sufficient growth. However, if the amount of precursor is not enough to dissipate all the non-uniformities during growth, intermediate structures such as truncated cuboids/octahedra could be obtained. Overall, tailoring the morphologies relies on tuning the PGDs and the properties of kinematic waves. We found that the cysteine in our system could play a role to change the PGDs from <111> to <100>, and accordingly tailoring the final morphologies. In such a system, the final shapes of Au@Ag NPs relied more on the growth processes themselves than the shape/size of the seeds, that is, Au seeds with different shapes could all be used to prepare cubes, octahedra, and tetrahedra. Cysteine could play an additional role as the chiral inducer. When the amount of $AgNO_3$ precursor was limited in the growth process to prohibit the full dissipation of all the non-uniformities via kinematic waves, dissymmetric truncated structures were obtained. Two different chiral forms were identified, which displayed opposite optical activities even though they were prepared with the same cysteine enantiomer (L-cys). The highest *g*-factor calculated according to the circular dichroism spectrum was ≈0.011, which was among the best reported chiral Au@Ag or Ag NPs to our knowledge. Finally, the chirality was probed by the electrooxidation of glucose, where the dissymmetric Au@Ag NPs behaved differently in D- and L-glucose solutions.

2. Results and Discussion

2.1. Tailoring the Symmetry of Au@Ag NP

The halide surfactant systems offer mild growth conditions (60–70 °C, 30 min to 3 h) toward the formation of Au@Ag NPs enclosed by {100} facets. Here we used different single-crystalline seeds (Figure S2 and Table S1, Supporting Information) to explore the shape diversities in the cetyltrimethylammonium chloride (CTAC) systems. $AgNO_3$ was used as the Ag precursor and ascorbic acid as the reducing agent. Cysteine was additionally used to tailor the shapes, and no other compounds were employed in our synthesis (see details in the Supporting Information). When Au nanorods (NRs, with an average length of 62.3 ± 4.2 nm and width of 16.9 ± 1.9 nm, denoted as Rod3) were used as seeds in the growth without cysteine, Au@Ag cuboids could be prepared. **Figure 1**a shows the products obtained with a $AgNO_3$ concentration of 0.25 mM and Au^0_{NR} seed concentration of 40 μM. On one hand, the thickness of the Ag shell could be adjusted by changing the feeding ratio between $AgNO_3$ and Au NR seeds (Figure S3, Supporting Information). However, if the feeding ratio of the $AgNO_3/Au^0_{NR}$ seed was too high, homogeneous nucleation would occur, leading to Ag nanoprisms and irregular shaped particles with grain boundaries (Figure S4, Supporting Information). On the other hand, the size of the Au@Ag cuboids could be additionally tailored by the size of the Au NR seeds (Figure S5, Supporting Information). If the size of the Au NR seeds was very small (with an average length of 11.6 ± 3.8 nm and width of 4.7 ± 0.7 nm, denoted as miniRod), Au@Ag cubes would be obtained (Figure 1b and Figure S6, Supporting Information). The obtained 36.5 nm Au@Ag cubes showed one main peak at 460 nm in the UV–vis–NIR spectrum, while the cuboids (with an average length of 71.2 nm and width of 34.1 nm) showed two intense peaks at 442 and 563 nm (Figure 1c). The spectra agree well with the simulations of ideal cubes and cuboids, suggesting the high uniformity of the synthesized particles (Figure S7a,b, Supporting Information).

Surprisingly, when cysteine was introduced into the growth with a concentration of 5 μM, the products would change from cuboids (Figure 1a) to octahedra (Figure 1d). The Au NR seeds could be clearly seen in the high-angle annular dark-field scanning transmission electron microscopy (HAADF-STEM) images. The octahedra with an average edge length of 43.7 nm showed a main peak at 482 nm in the UV–vis–NIR spectrum, which was consistent with the simulations (Figure S7c, Supporting Information). When the sizes of the Au NR seeds changed, octahedra could be obtained by slightly adjusting the $AgNO_3$ concentrations (Figure S8, Supporting Information).

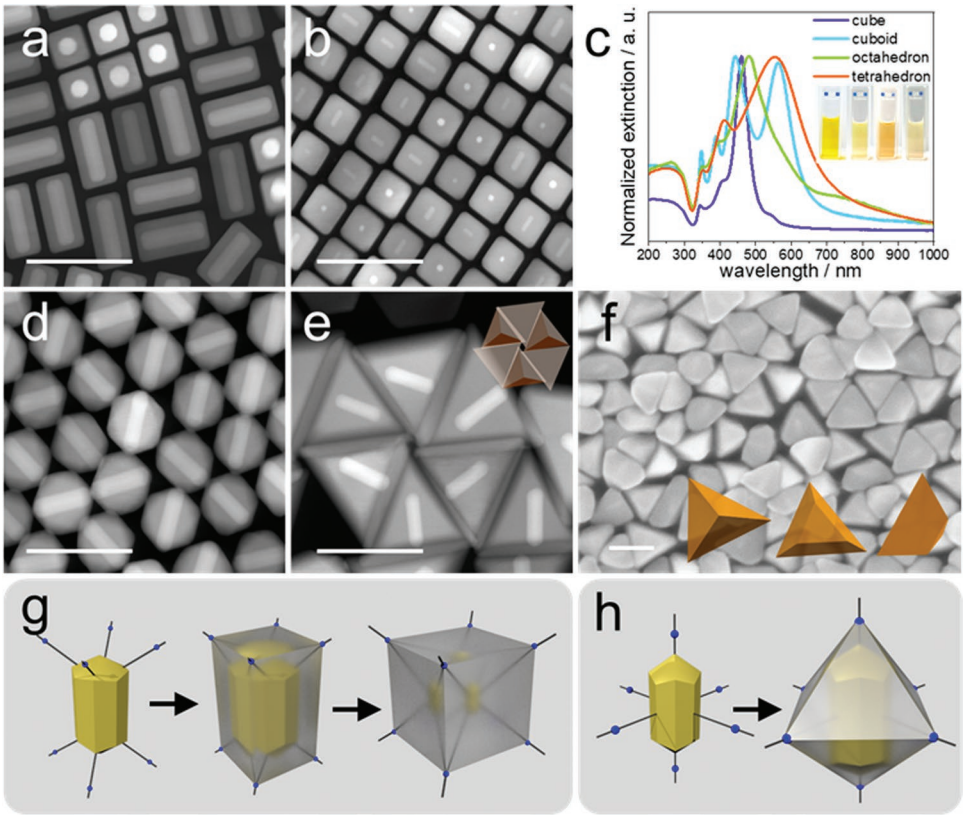

Figure 1. a) STEM images of the Au@Ag cuboids, some particles are standing while most of the particles lie flat on the TEM grid. b) Cubes. c) Normalized UV–vis–NIR spectra of these particles. The inset shows the optical images of the particles (from left to right: cube, cuboid, octahedron, tetrahedron). d) Octahedra. e) Tetrahedra, the inset shows a pinwheel packing of six tetrahedra, which resemble the observed pattern. f) The scanning electron microscopy (SEM) image shows a gallery of tetrahedra and truncated tetrahedra. The inset shows some models of the tetrahedra and truncated tetrahedra. All scale bars: 100 nm. g,h) The evolution from a rod to a cuboid/cube and an octahedron, respectively. The black lines indicate the <111> or <100> directions of the rod (PGDs), and the blue dots mark the crystallographically equivalent sites at these directions. The blue dots can also be considered as the nucleation sites of the growth fronts. By connecting these points, the evolved shape could be depicted.

Once the $AgNO_3$ concentrations greatly exceeded these levels, Au@Ag tetrahedra and truncated tetrahedra were obtained (Figure 1e,f and Figure S9, Supporting Information). To date, there are very limited reports on the preparation of Ag[12] or Au@Ag tetrahedra,[33] regardless of the versatile properties of the tetrahedra.[34–36] Light is typically adopted to assist the tetrahedron growth. Therefore, we sought to gain insights into the formation of tetrahedra, as well as other obtained shapes, to provide a comprehensive understanding.

2.2. Interrogating the Morphology Control via the SBKT

The role of cysteine in such a system might be complicated since the $-NH_2$ group and $-SH$ group in the cysteine could all firmly bind with the Ag^+ and the surface Ag atoms. As the concentration of cysteine was greatly lower than that of the Ag^+, and comparable to the surface atoms of the NP, we tended to suppose that the cysteine played a role mainly by surface adsorption, that is, by influencing the crystal growth behavior, but not forming Ag^+–cysteine complexes. In addition, Ag^+ would react with Cl^- in the system to form Ag–Cl compounds first, and then convert to metallic Ag shells.[9,14,15] Thus, CH_3COOAg could also serve as the precursor in this system (Figure S10, Supporting Information). These results suggested that the role of each compound might be coupled, and understanding the role of each one might be difficult. Then we tried to use the SBKT to understand the shape evolutions because the SBKT focuses more on the crystal growth behavior than the explicit role of each component.[31,32] When cysteine was excluded in the synthesis, the PGDs of the system could be assigned to the <111> directions according to the crystallography of the final products (particles enclosed by {100} facets feature <111> PGDs). The rod seed could then be put into a virtual coordination system, and the crystallographically equivalent sites are labeled (Figure 1g), which can also be seen as the nucleation sites of the growth fronts. By connecting these equivalent sites, a cuboid shape could be obtained.[32] However, the cuboid is an anisotropic structure featuring a $4/mmm$ symmetry, which does not conform to the lattice symmetry $\left(\frac{4}{m}\bar{3}\frac{2}{m}\right)$, that is, the particle contains non-uniformity. Accordingly, the kinematic wave would propagate through all the surfaces of the particles to dissipate all the non-uniformity, finally evolving to a particle with a $\frac{4}{m}\bar{3}\frac{2}{m}$ symmetry (cubes since the PGDs are <111> in this

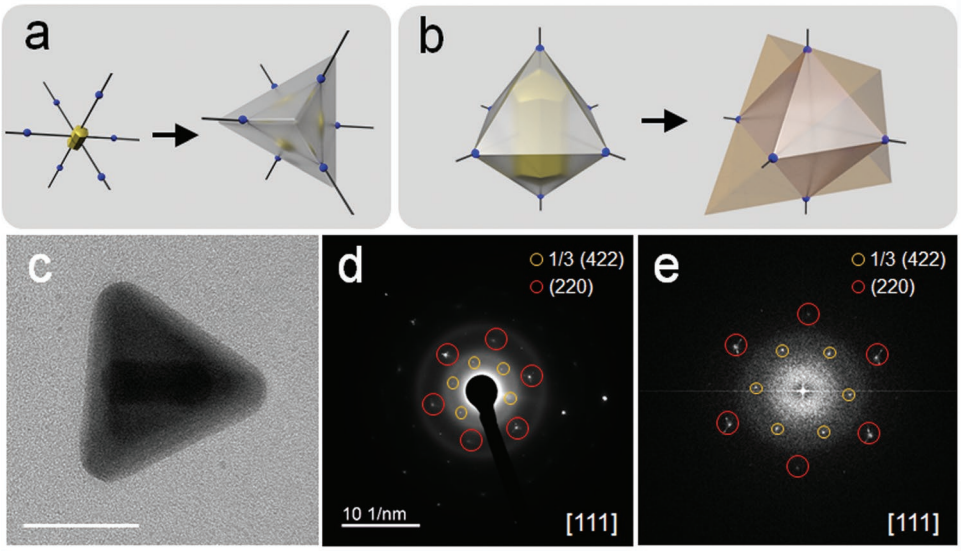

Figure 2. a) A scheme showing the evolution of a single-crystalline tetrahedron according to the SBKT. The black lines indicate the <100> direction (PGDs), and the blue dots mark the crystallographically equivalent sites at these directions. If the nucleation sites are edges rather than corners as those shown in Figure 1g,h, a tetrahedron should be obtained. b) A scheme showing the evolution from an octahedron to a tetrahedron. The detailed evolution principle can be found in Figure S12, Supporting Information. c) TEM image of a tetrahedron for SAED (d) and FFT (e) analysis. The scale bar is 50 nm. Images with higher magnification can be found at Figure S11, Supporting Information. d,e) The orange dots mark the 1/3 (422) reflections. Such spots are forbidden in the diffraction patterns of the single crystalline fcc lattice. The existence of these spots suggests twinning perpendicular to a {111} face of the tetrahedron.[33,39,40] The red dots mark the (220) reflections. The dots are split as a result of the existence of a twin plane. Since the *d*-spacings of Ag (220) and Au (220) are nearly identical (1.4447 and 1.4418 Å, respectively), the Au (220) spots are indistinguishable from those of Ag (220).

case) after sufficient growth. When the seed size is large, the kinematic wave needs to consume lots of Ag precursors during its propagation through the whole surface. Thus, cuboids could be obtained when the amount of Ag precursors is not sufficient (Figure 1a). On the contrary, cubes could be easily obtained with small sized seeds since the kinematic wave only needs to consume a smaller amount of precursors to fully dissipate the non-uniformities (Figure 1b). When cysteine was included in the synthesis, the PGDs would be changed to <100> directions according to the crystallography of the final products. Doing the same analyses, the evolution of an octahedron can be understood when the growth is sufficient (Figure 1h, shapes without sufficient growth will be analyzed in the later discussions on the chiral particles).

According to the SBKT, a tetrahedron could be foreseen with <100> PGDs and edge nucleation sites (not corner nucleation sites as discussed above) (**Figure 2**a). Since a tetrahedron features a $\bar{4}3m$ symmetry, it should evolve to an octahedron after sufficient growth. However, the experimental results suggested that more Ag precursors lead to a tetrahedron, not the other way around. This apparent contradiction is because the obtained tetrahedra are not single-crystalline, while the SBKT retrieves the symmetry from the single-crystalline lattice for further analysis. The selected-area electron diffraction (SAED) patterns and the fast Fourier transform (FFT) patterns of the high-resolution TEM images suggested that the obtained tetrahedra contain twin faults (Figure 2c–e and Figure S11, Supporting Information). The formation of twin defects could break the symmetry of the lattice, and also change the surface nucleation rates at different sites. Consequently, the SBKT analysis needs to be modified. The single-crystalline Au NR seeds could serve as the TEM labels to illustrate that the core of the tetrahedron is single-crystalline,[33] which also means no twin faults should be created at the early stage of the growth. With <100> PGDs and considering the properties of the kinematic waves, octahedra should be formed at the early stage. Once the size of the octahedra exceeds the level to fully encapsulate the single-crystalline Au NR seeds, twin faults are allowed to form. The formed twin faults could, on one hand, serve as self-perpetuating sites to provide surface nucleation sites to enlarge the particles,[37,38] and on the other hand, to limit the shape into a tetrahedron (Figure 2b and Figure S12, Supporting Information).

The shape evolution during the growth can be depicted by the PGDs and the properties of the kinematic waves which are defined by the growth conditions, while the seeds provide an initial structure for the initiation of the kinematic waves. Therefore, we tried to explore the growth with differently shaped seeds. When cuboctahedra were used as seeds, octahedra and tetrahedra could be obtained at different $AgNO_3$ concentrations in the presence of cysteine (**Figure 3**a–c and Figure S13, Supporting Information). The tetrahedra also contained twin faults, the same as the tetrahedra prepared with NR seeds (Figure S13e,f, Supporting Information). Meanwhile, the amount of truncated tetrahedra was quite low in the final products (Figure S11c,d, Supporting Information). We further used Au dendrimers as an example of irregularly shaped seeds to test the robustness of the growth system. The results showed the same shape transition trends, that is, Au@Ag cubes would be obtained without cysteine, and more $AgNO_3$ could shift the octahedra to tetrahedra in the existence of cysteine (Figure 3d–g and Figure S14, Supporting Information). Therefore, such a growth system is quite robust, the output morphology relies

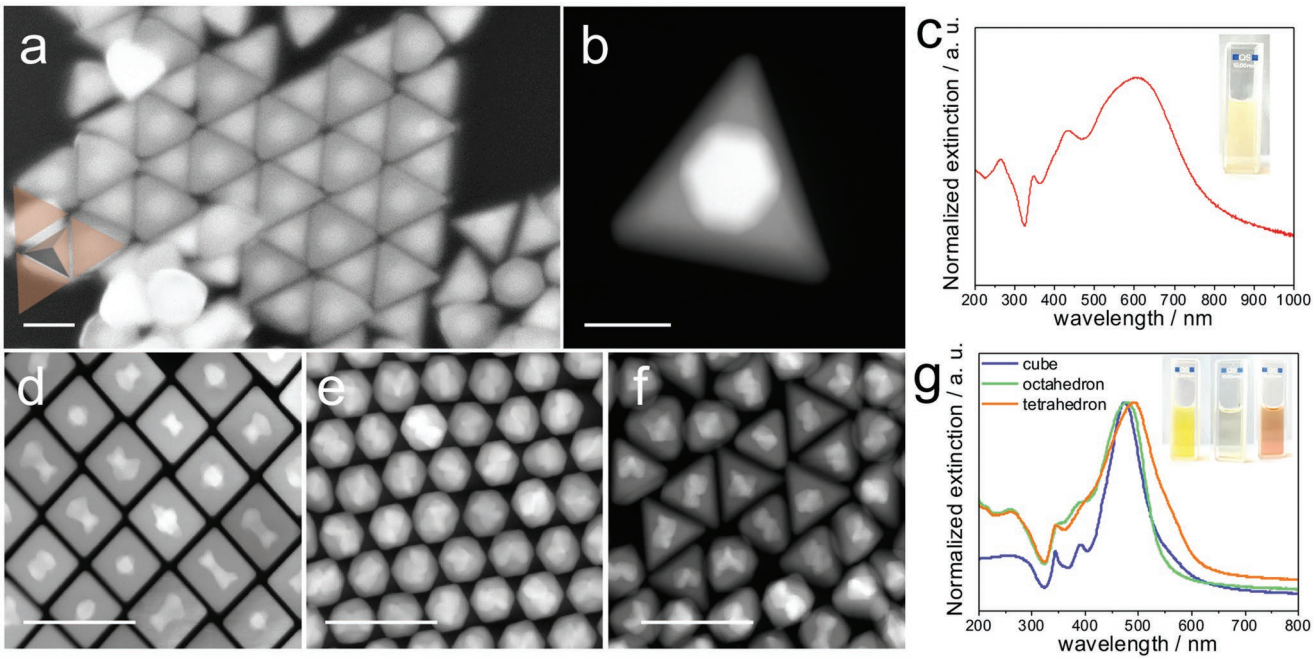

Figure 3. a) Scanning electron microscopy (SEM) image, b) STEM image, and c) extinction spectrum of the tetrahedra prepared with cuboctahedra as seeds in the presence of cysteine. d–f) STEM images of cubes, octahedra, and tetrahedra prepared with Au dendrimers as seeds (cubes were prepared without L-cys, octahedra and tetrahedra were prepared with L-cys concentration of 5 μM), as well as their corresponding extinction spectra (g). The inset of (g) shows the optical images of the particles (from left to right: cube, octahedron, tetrahedron). Scale bars: 100 nm (a,d–f) and 50 nm (b), respectively.

more on the growth conditions (ratio between $AgNO_3$ and Au^0 seeds, cysteine) than the shapes of the input seeds.

2.3. Dissymmetric Synthesis

Since chiral cysteine (L-cys in the above discussions) was used in the synthesis and it played a significant role to tune the final shapes, it would be interesting to see whether chiral Au@Ag NPs could be prepared in such a system and what could be the chiral forms of the NPs. Noting that the term "dissymmetry" is used in crystallography as early as 1820 and later became a synonym for "chirality" during the development of concepts and nomenclatures in stereochemistry (Louis Pasteur used "dissymmetry" in his famous experiments on the tartrates in 1848, and Sir William Thomson, known as Lord Kelvin, coined the term "chirality" in 1894),[41] but "dissymmetry" or "dissymmetric" is less used in the past decades, it might be appropriate to use "dissymmetric synthesis" to refer to the growth of chiral NPs or crystals, as their formation mechanism is apparently different to those of chiral molecules, for which the term "asymmetric synthesis" is widely accepted. According to the SBKT, the non-uniformities within the NPs tend to disappear after sufficient growth, while chiral NPs obviously contain non-uniformities since chiral NPs would never adopt a $\frac{4}{m}\bar{3}\frac{2}{m}$ symmetry. Indeed, the obtained octahedra showed no optical activities (Figure S15a, Supporting Information). Thus, the Ag precursor feeding should be at least reduced, to preserve the non-uniformities. When the concentration of $AgNO_3$ was decreased from 0.25 to 0.1 mM, while other conditions remained the same as those in the preparation of Au@Ag octahedra, not surprisingly, truncated octahedra were prepared (**Figure 4**a and Figure S16, Supporting Information). The particles showed optical activities as evidenced by the circular dichroism spectrum, which meant the particles were dissymmetric, even though very weakly (a very low *g*-factor maximum of ≈0.0015) (Figure S17, Supporting Information). This result encouraged us to explore the chiral forms of the Au@Ag NPs. A tetrahedron with four corners differently truncated has already been demonstrated to be chiral[42] (Figure 4b). Similarly, an octahedron with four corners differently truncated should also be chiral (Figure 4c). Figure 4a and Figure S16, Supporting Information, demonstrate that the octahedra were truncated, and the truncations were no smooth surfaces. Thus, the four corners might be not equally truncated, and the NP should be dissymmetric, which is consistent with the circular dichroism spectrum. Furthermore, the truncations cannot be assigned to low index facets. In materials with an fcc lattice, facets with index of $h \neq k \neq l$ and $h \times k \times l \neq 0$ are atomically chiral.[43] When the amounts of the enantiomeric chiral facets within a particle are not equal (the amount of R-type facets ≠ S-type facets), the particle should be dissymmetric.[21] It has been confirmed that L-cys could enantioselectively assist the formation of chiral facets during the growth of Au NPs,[18,23,44,45] resulting in the controlled growth of chiral NPs. The L-cys in our case might function similarly as the chiral inducer to control the chirality, resulting in reproducible chiral NPs.

Then we sought to enhance the dissymmetry of the truncated octahedra from the perspective of growth mechanism. During the evolution of an Au NR to an Au@Ag octahedron,

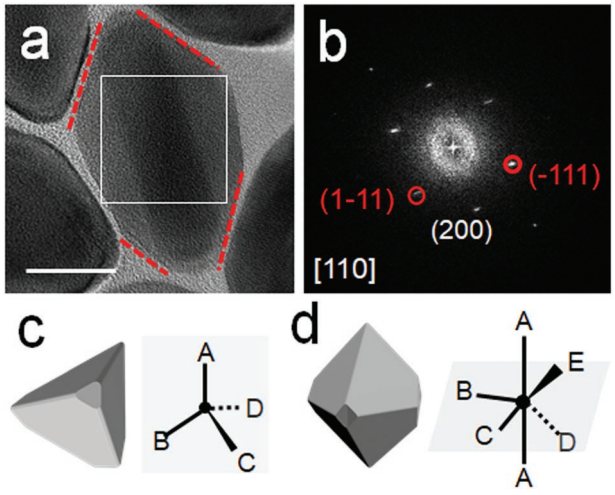

Figure 4. a) High-resolution TEM (HRTEM) image of the truncated octahedra (scale bar: 20 nm). The FFT pattern of the white frame area is shown in (b). By analyzing the FFT patterns, the {111} facets of the truncated octahedra are labeled by the red dashed lines. The analysis method is shown in Figure S16, Supporting Information. c,d) The truncated tetrahedron and octahedron can be abstracted to the sketches shown in the right, by considering the relative positions of the truncation centers to the particle center. If (A)–(E) are not equal (due to different truncation shapes, different distances to the center, etc.), no mirror planes and inverse centers could be found in these structures. Therefore, the particles are chiral.

the Ag atoms would undergo surface nucleation on the Au NR followed by the layer advancements of Ag layers (2D surface nuclei) to enlarge the particles. With the help of kinematic waves to dissipate all the non-uniformities, a well-defined octahedron would be anticipated after sufficient growth without needing to know the detailed growth processes (**Figure 5**a). To understand the formation of intermediate structures such as truncated shapes, the detailed growth processes need to be evaluated (Figure 5b). After the surface nucleation of Ag atoms, non-uniformity such as steps would be created spontaneously. Then the kinematic wave would start to propagate through the whole particles, accompanied by the consumption of Ag precursors. Once the Ag precursors are depleted, the growth would stop and the final shape of a particle would be fixed. Meanwhile, the existence of L-cys might terminate the facet development in a chiral manner, leading to the exposition of chiral surfaces.[32] Therefore, the dissymmetry of the products should be related to the surface areas of the seeds since larger surface area means that it is more difficult for the kinematic waves to fully dissipate all the non-uniformities of the particles during the growth. Meanwhile, the seeds provide the initial structure for the kinematic wave propagation, so the anisotropy of the seeds (i.e., the aspect ratio, AR) should also be accounted for. Altogether, the dissymmetry of the final product should be related with both the surface area and the AR of the seeds:

$$\text{dissymmetry} \propto f(\text{length} \times \text{width}) \times g(\text{length}/\text{width}) \quad (1)$$

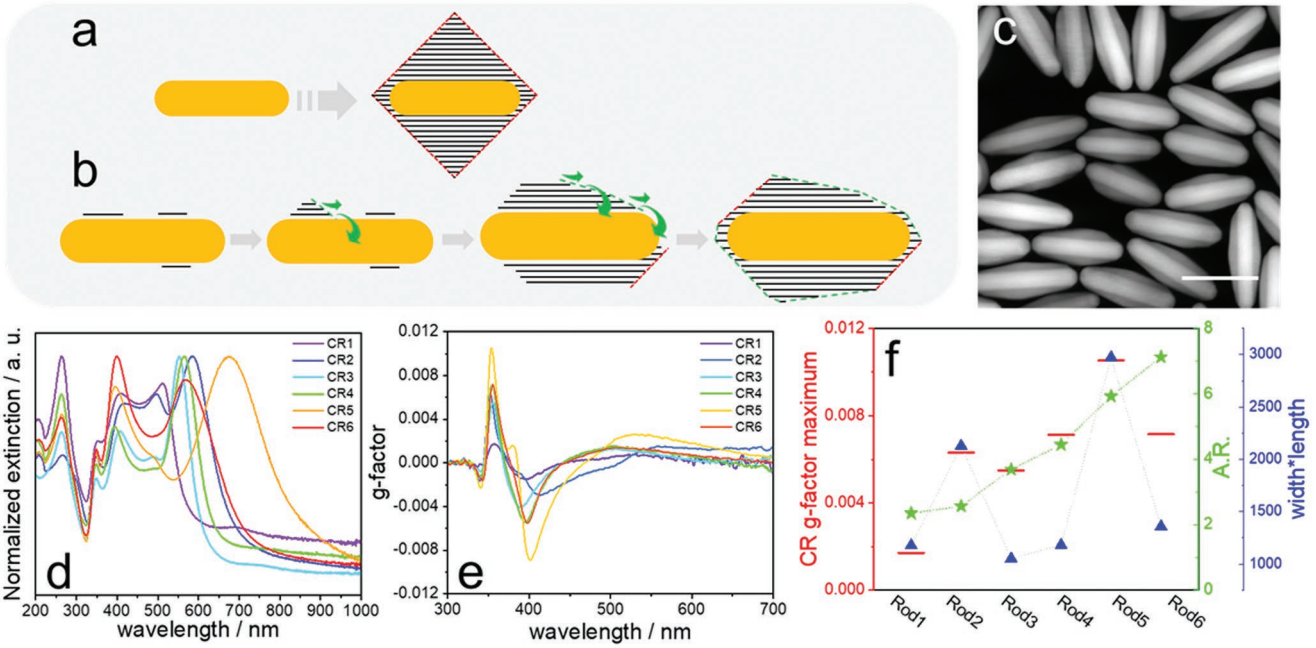

Figure 5. a) Simplified 2D sketches of the formation of an Au@Ag octahedron. b) The intermediate steps in (a). The black lines stand for the Ag atom layers, while the red dashed lines denote the {111} facets. The Ag atom layers are formed on the surface of the Au NR via a surface nucleation process, and then surface non-uniformity would be created (green dashed lines). Such non-uniformity would propagate to other regions in the form of kinematic waves (green arrows) during the growth, accompanying the enlargement of the particle and the consumption of the Ag precursors. c) STEM images of the chiral rod 5 (CR5) (scale bar: 100 nm). d,e) Extinction spectra and *g*-factor plots of various chiral rods, after optimized growth conditions in each case. f) Relationship between the CR *g*-factor maximum and the dimensions of the rod seeds.

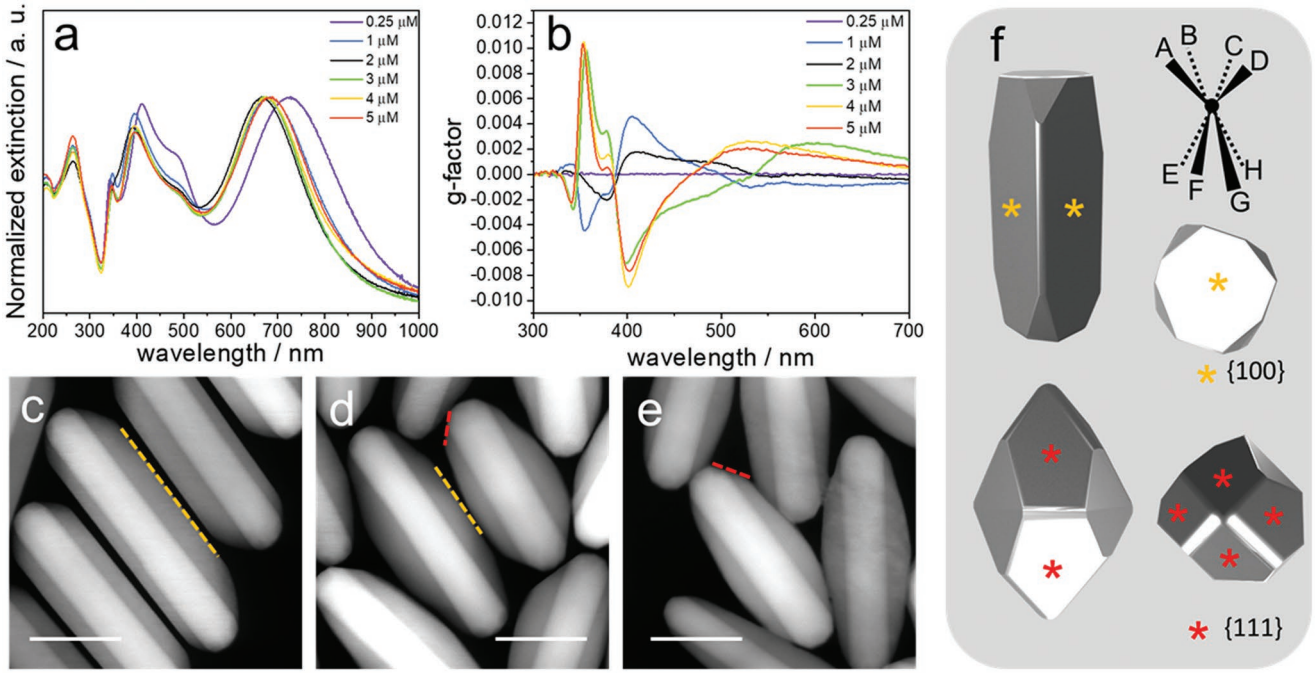

Figure 6. a,b) Extinction spectra and *g*-factor plots of the chiral rods obtained with different L-cys concentrations. The seeds were Rod5. c–e) STEM images of the CRs obtained with L-cys concentration of 1, 2, and 3 μM, respectively. The dashed orange lines mark the {100} facets, while the red dashed lines mark the {111} facets. The facet analysis method can be found in Figure S24, Supporting Information. These low-index facets are the achiral surfaces. The results also suggested that morphologies in (c) are truncated cuboids, while in (e) are truncated octahedra. f) If the relevant corners of the cuboid and the octahedron are not equally truncated, the particles should be chiral.

Bearing this in mind, we started to optimize the growth conditions for dissymmetric NPs and explore the relationship between the dissymmetry and the seeds. The benzyldimethylhexadecylammonium chloride (BDAC) surfactant system was found to be more advantageous in realizing higher *g*-factors than CTAC or cetylpyridinium chloride surfactant systems (Figure S17, Supporting Information), and therefore was used in the following optimizations. By carefully adjusting the concentrations of $AgNO_3$, L-cys, and Au^0_{NR} seeds, the optimized growth conditions for each size of Au NR seeds were found (Figures S18 and S19, Supporting Information). The extinction spectra and *g*-factor spectra of the optimized products were then plotted (Figure 5d,e). The extinction spectra of these chiral rods (CR) showed similar features, with several peaks centered at ≈264, ≈348, and 390–400 nm, and a peak at a longer wavelength depending on the AR of the CR. The shapes of the *g*-factor spectra were also similar, with one main positive peak at ≈354 nm, one main negative peak at 390–400 nm, and several other weaker peaks. The main positive peaks were more intense than the negative peaks. These suggested that the shapes of the obtained CR were quite similar, that is, truncated octahedra (Figure 5c and Figures S20 and S21, Supporting Information). The strongest *g*-factor of each CR was then recorded as an indicator of the dissymmetry of the final products, and then compared with the initial sizes of the Au NR seeds (Figure 5f). For rods with comparable surface areas (length × width), such as Rod1, Rod3, Rod4, and Rod6, higher AR could result in CR with a larger *g*-factor maximum. For rods with similar AR, such as Rod1 and Rod2, larger surface areas would lead to significantly higher *g*-factors. Rod5 which features a smaller AR than Rod6 but a much larger surface area displayed the maximal *g*-factor of 0.011. Au spheres (AR ≈ 1) and minirods (small surface areas) were also tested as seeds for chiral growth, but no optical activities were found for our growth conditions (data not shown). These trends generally obey the Equation (1). It is also worth noting that the *g*-factor maxima here are generally higher than those reported in literature (Table S2, Supporting Information). When D-cys was used in the synthesis, symmetric *g*-factor plots were recorded (Figure S22a, Supporting Information), while the extinction spectra and the morphologies of the CR were quite similar (Figure S22b–e, Supporting Information).

Another interesting phenomenon we found was that the optical activities of the CR would be reversed when the concentration of L-cys was decreased, although their extinction spectra were quite similar (**Figure 6**a,b). When L-cys was included in the synthesis, the extinction spectra showed several peaks at ≈264, ≈348, 396–410, ≈488 (shoulder peak), and 665–730 nm. When the L-cys concentrations were lower than 2 μM, the extinction peaks centered at 396–410 and 665–730 nm will blueshift as the L-cys concentration increased. When the L-cys concentrations were higher than 2 μM, these peaks would then slightly redshift as the L-cys concentration increased. In the *g*-factor plots (Figure 6b), several peaks existed (≈342, ≈354, ≈378, ≈405, and >500 nm [a broad peak]). The signs of all the peaks were reversed at L-cys concentrations below and above 2 μM, even though the particles were prepared with the same enantiomer. The peak intensities were generally higher with L-cys concentrations higher than 2 μM. The reason of the

optical activity inversion should be associated with the changes of the chiral forms (Figure 6c–e and Figure S23, Supporting Information). With L-cys concentration of 1 μM, cuboids with corners differently truncated were the chiral form (Figure 6c,f and Figure S24a–c, Supporting Information). With L-cys concentration of 3 μM, truncated octahedra were in the chiral form (Figure 6e,f and Figure S22d–f, Supporting Information), while a mixture of chiral truncated cuboids and octahedra could be found at the L-cys concentration of 2 μM (Figure 6d). We suspect that the inversion is due to the changes of the chiral sites. The chirality originates from the corner truncations, which reside at the CR tips of the truncated cuboid, while at the CR middle parts of the truncated octahedron. The inversion of the chiral parts might lead to the inversed optical activities. These phenomena were also found with other sized Au NR seeds (Figure S25, Supporting Information). Altogether, two different kinds of Au@Ag chiral forms were identified in this research.

2.4. Enantioselective Electrochemical Glucose Oxidation

Finally, the NPs were probed by electrochemistry. Electrochemistry is a very sensitive method to distinguish the surface differences of the NPs.[46] The electrochemical surface areas (ECSA) of the achiral NPs (cuboid, octahedron) and chiral NPs (CR3, CR4, CR5) were measured by the Pb underpotential deposition (UPD) technique (Table S3, Supporting Information).[46–48] The oxidation leaching of the Pb UPD layer is shown in **Figure 7**a. The results showed that achiral and chiral NPs displayed different leaching behavior, suggesting that their surface features were different. For cuboids, a narrow peak at 0.31 V (vs reversible hydrogen electrode (RHE)) was found, while a broad peak centered at 0.28 V and several shoulder peaks could be found for octahedra. Chiral NPs exhibited broad leaching peaks at 0.30 V. Then glucose was used as a probe to investigate the chirality. The enantiomeric electro-oxidation of D- and L-glucose has been found on a chiral Au surface, in which the corresponding enantioselectivity factor was estimated to be 10% for the process occurring at lower potential values and to 50% for the process at higher potential values.[49] Such a reaction has not been carefully examined on chiral Ag surfaces to date. The Au surface does not need to be oxidized to deliver the selectivity.[50] However, the Ag surface needs to be at least partially oxidized to Ag_2O or AgO to drive the glucose oxidation.[51,52] Nonetheless, the chiral NPs here showed selectivity in different glucose solutions according to the cyclic voltammetry (CV) scans, while achiral NPs showed nearly no difference (Figure 7b–d and Figures S26 and S27, Supporting Information). The slightly changed curves of the achiral NPs in D- and L-glucose solutions could be attributed to the irreversibility of the Ag oxidation–reduction cycles.[51] But the irreversibility was not adequate to explain the marked changes in chiral NPs (Figure S28, Supporting Information). We focused on the negative peaks at 0.95–1 V to demonstrate the selectivity as a proof-of-concept.

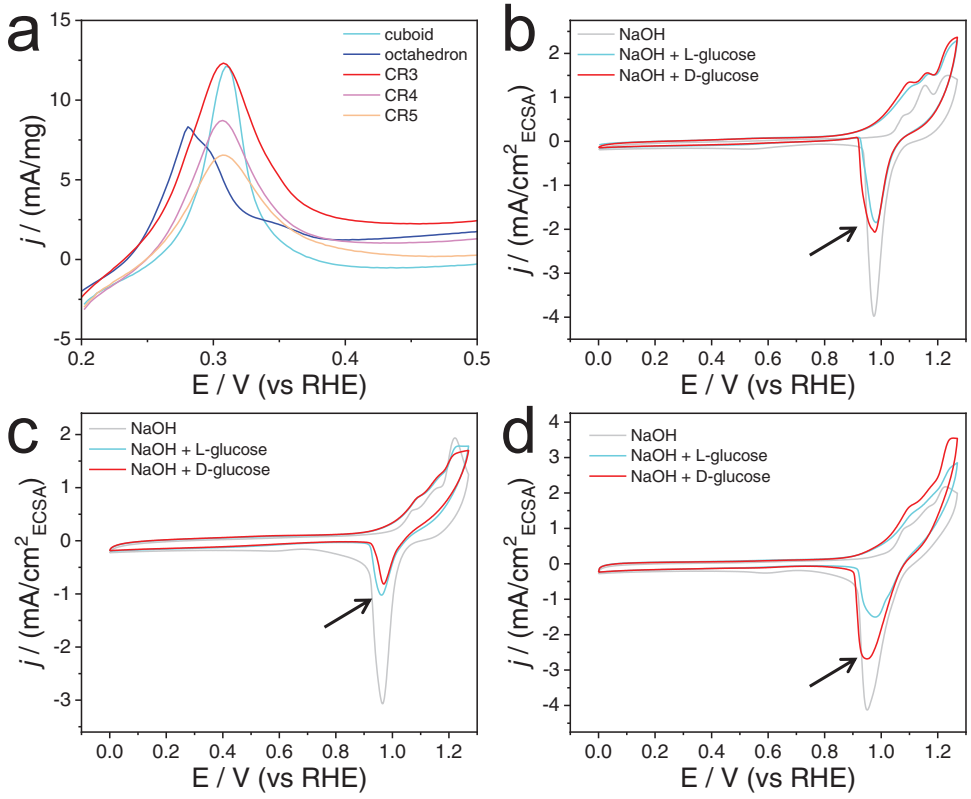

Figure 7. a) Oxidative leaching of the Pb UDP layers. b–d) The current densities are normalized to the mass loading of the Au@Ag NPs. CV scans of the Au@Ag cuboids (b), octahedra (c), and CR5 (d) in different solutions. The concentrations of NaOH are 0.1 M, and L- (or D-) glucose are 0.01 M. The black arrows point to the peaks of interest in illustrating the enantioselectivity.

The reason to the current density decrease in glucose solutions when compared to pure NaOH solutions could be attributed to the glucose oxidation together with less Ag oxidation during the positive scan. Such decrease was used to calculate the selectivity (Table S4, Supporting Information), and a selectivity of ≈28.9% was found with CR5. The value could already demonstrate a proof-of-concept that chiral Au@Ag NPs could deliver enantioselectivity toward glucose oxidation.

3. Conclusion

We have demonstrated a facile method to tailor the morphologies of the Au@Ag NPs, and accordingly the NP symmetry would be also regulated. The method relies on the seed-mediated growth of Ag shells on Au seeds in the halide surfactant system. When cysteine is included in the synthesis, the morphologies would change from cubes/cuboids $\left(\frac{4}{m}\bar{3}\frac{2}{m}\right)$ and 4/*mmm* symmetry, respectively) to octahedra $\left(\frac{4}{m}\bar{3}\frac{2}{m}\right)$, and finally to tetrahedra ($\bar{4}3m$) when the Ag precursor is also increased. The cubes/cuboids and octahedra are single-crystalline, while the tetrahedra contain twin faults. The system is quite robust where differently shaped NPs or irregular NPs could all be used as seeds to prepare uniform Au@Ag NPs, and the rules to regulate the morphologies remain the same. The evolution of these shapes could be comprehensively understood by the SBKT. Guiding by principles derived from the SBKT analysis, chiral Au@Ag NPs are successfully prepared and optimized via a dissymmetric synthesis. The strongest *g*-factor we obtained is ≈0.011, which is among the best of the reported results. In addition, two chiral forms (truncated cuboids and octahedra) with different chiral features are also identified. The chirality originates from the tips and middle parts of the CR in the truncated cuboids and octahedra. The reversion of the dissymmetric parts might lead to the reversion of the optical activities. Finally, the electro-oxidation of glucose suggested that the chiral NPs could show enantioselectivity, whereas the chiral NPs showed different behavior in D- and L-glucose solutions. The method developed here could provide a facile method to prepare Au@Ag NPs with high shape and size uniformities for further research, and also the two chiral forms of Au@Ag NPs could pave a way for wider investigations of plasmonic chirality or inorganic chirality, as well as dissymmetric synthesis.

Supporting Information

Supporting Information is available from the Wiley Online Library or from the author.

Acknowledgements

The authors thank Prof. Peter Baum for the help with the optical simulations. B.N. acknowledges a postdoctoral fellowship of the Alexander von Humboldt Foundation. H.C. thanks Deutsche Forschungsgemeinschaft (DFG) SFB 1214 project B1 for funding.

Open access funding enabled and organized by Projekt DEAL.

Conflict of Interest

The authors declare no conflict of interest.

Data Availability Statement

The data that support the findings of this study are available from the corresponding author upon reasonable request.

Keywords

Au@Ag nanoparticles, chiral truncated particles, dissymmetric synthesis, enantioselective glucose oxidation, morphology control, symmetry-based kinematic theory

Received: October 24, 2022
Revised: December 5, 2022
Published online: March 4, 2023

[1] Q. Zhang, W. Li, C. Moran, J. Zeng, J. Chen, L.-P. Wen, Y. Xia, *J. Am. Chem. Soc.* **2010**, *132*, 11372.
[2] A. Kumar, P. K. Vemula, P. M. Ajayan, G. John, *Nat. Mater.* **2008**, *7*, 236.
[3] M. K. Rai, S. D. Deshmukh, A. P. Ingle, A. K. Gade, *J. Appl. Microbiol.* **2012**, *112*, 841.
[4] M. Rycenga, X. Xia, C. H. Moran, F. Zhou, D. Qin, Z.-Y. Li, Y. Xia, *Angew. Chem., Int. Ed.* **2011**, *50*, 5473.
[5] M. Rycenga, C. M. Cobley, J. Zeng, W. Li, C. H. Moran, Q. Zhang, D. Qin, Y. Xia, *Chem. Rev.* **2011**, *111*, 3669.
[6] Y. Shi, Z. Lyu, M. Zhao, R. Chen, Q. N. Nguyen, Y. Xia, *Chem. Rev.* **2021**, *121*, 649.
[7] T. Pu, H. Tian, M. E. Ford, S. Rangarajan, I. E. Wachs, *ACS Catal.* **2019**, *9*, 10727.
[8] B. Wiley, Y. Sun, Y. Xia, *Acc. Chem. Res.* **2007**, *40*, 1067.
[9] S. Zhou, J. Li, K. D. Gilroy, J. Tao, C. Zhu, X. Yang, X. Sun, Y. Xia, *ACS Nano* **2016**, *10*, 9861.
[10] R. Jin, Y. C. Cao, E. Hao, G. S. Métraux, G. C. Schatz, C. A. Mirkin, *Nature* **2003**, *425*, 487.
[11] J. Zhang, M. R. Langille, C. A. Mirkin, *Nano Lett.* **2011**, *11*, 2495.
[12] J. Zhou, J. An, B. Tang, S. Xu, Y. Cao, B. Zhao, W. Xu, J. Chang, J. R. Lombardi, *Langmuir* **2008**, *24*, 10407.
[13] Y. Xia, K. D. Gilroy, H.-C. Peng, X. Xia, *Angew. Chem., Int. Ed.* **2017**, *56*, 60.
[14] S. Gómez-Graña, B. Goris, T. Altantzis, C. Fernández-López, E. Carbó-Argibay, A. Guerrero-Martínez, N. Almora-Barrios, N. López, I. Pastoriza-Santos, J. Pérez-Juste, S. Bals, G. Van Tendeloo, L. M. Liz-Marzán, *J. Phys. Chem. Lett.* **2013**, *4*, 2209.
[15] K. Park, L. F. Drummy, R. A. Vaia, *J. Mater. Chem.* **2011**, *21*, 15608.
[16] G. Zheng, S. Jiao, W. Zhang, S. Wang, Q. Zhang, L. Gu, W. Ye, J. Li, X. Ren, Z. Zhang, K.-y. Wong, *Nano Res.* **2022**, *15*, 6574.
[17] A. Carone, P. Mariani, A. Désert, M. Romanelli, J. Marcheselli, M. Garavelli, S. Corni, I. Rivalta, S. Parola, *ACS Nano* **2022**, *16*, 1089.
[18] H.-E. Lee, H.-Y. Ahn, J. Mun, Y. Y. Lee, M. Kim, N. H. Cho, K. Chang, W. S. Kim, J. Rho, K. T. Nam, *Nature* **2018**, *556*, 360.
[19] G. González-Rubio, J. Mosquera, V. Kumar, A. Pedrazo-Tardajos, P. Llombart, D. M. Solís, I. Lobato, E. G. Noya, A. Guerrero-Martínez, J. M. Taboada, F. Obelleiro, L. G. MacDowell, S. Bals, L. M. Liz-Marzán, *Science* **2020**, *368*, 1472.
[20] L. Xu, X. Wang, W. Wang, M. Sun, W. J. Choi, J.-Y. Kim, C. Hao, S. Li, A. Qu, M. Lu, X. Wu, F. M. Colombari, W. R. Gomes, A. L. Blanco,

A. F. de Moura, X. Guo, H. Kuang, N. A. Kotov, C. Xu, *Nature* **2022**, *601*, 366.
[21] B. Ni, M. Mychinko, S. Gómez-Graña, J. Morales-Vidal, M. Obelleiro-Liz, W. Heyvaert, D. Vila-Liarte, X. Zhuo, W. Albrecht, G. Zheng, G. González-Rubio, J. M. Taboada, F. Obelleiro, N. López, J. Pérez-Juste, I. Pastoriza-Santos, H. Cölfen, S. Bals, L. M. Liz-Marzán, *Adv. Mater.* **2022**, *n/a*, 2208299.
[22] N. A. Kotov, L. M. Liz-Marzán, Q. Wang, *Mater. Adv.* **2022**, *3*, 3677.
[23] G. Zheng, J. He, V. Kumar, S. Wang, I. Pastoriza-Santos, J. Pérez-Juste, L. M. Liz-Marzán, K.-Y. Wong, *Chem. Soc. Rev.* **2021**, *50*, 3738.
[24] J. Cai, W. Zhang, L. Xu, C. Hao, W. Ma, M. Sun, X. Wu, X. Qin, F. M. Colombari, A. F. de Moura, J. Xu, M. C. Silva, E. B. Carneiro-Neto, W. R. Gomes, R. A. L. Vallée, E. C. Pereira, X. Liu, C. Xu, R. Klajn, N. A. Kotov, H. Kuang, *Nat. Nanotechnol.* **2022**, *17*, 408.
[25] G. Shemer, O. Krichevski, G. Markovich, T. Molotsky, I. Lubitz, A. B. Kotlyar, *J. Am. Chem. Soc.* **2006**, *128*, 11006.
[26] J. Xie, Y. Duan, S. Che, *Adv. Funct. Mater.* **2012**, *22*, 3784.
[27] B. M. Maoz, R. van der Weegen, Z. Fan, A. O. Govorov, G. Ellestad, N. Berova, E. W. Meijer, G. Markovich, *J. Am. Chem. Soc.* **2012**, *134*, 17807.
[28] B. Ni, H. Cölfen, *SmartMat* **2021**, *2*, 17.
[29] Y. Zhao, L. Cui, W. Ke, F. Zheng, X. Li, *ACS Sustainable Chem. Eng.* **2019**, *7*, 5157.
[30] T. Yasukawa, H. Miyamura, S. Kobayashi, *J. Am. Chem. Soc.* **2012**, *134*, 16963.
[31] B. Ni, G. González-Rubio, F. Kirner, S. Zhang, H. Cölfen, *Angew. Chem., Int. Ed.* **2022**, *61*, e202200753.
[32] B. Ni, G. González-Rubio, H. Cölfen, *ChemPhysChem* **2022**, *24*, 202200480.
[33] M. R. Langille, J. Zhang, M. L. Personick, S. Li, C. A. Mirkin, *Science* **2012**, *337*, 954.
[34] A. Haji-Akbari, M. Engel, A. S. Keys, X. Zheng, R. G. Petschek, P. Palffy-Muhoray, S. C. Glotzer, *Nature* **2009**, *462*, 773.
[35] P. F. Damasceno, M. Engel, S. C. Glotzer, *Science* **2012**, *337*, 453.
[36] Z. Cheng, M. R. Jones, *Nat. Commun.* **2022**, *13*, 4207.
[37] R. W. Berriman, R. H. Herz, *Nature* **1957**, *180*, 293.
[38] D. R. Hamilton, R. G. Seidensticker, *J. Appl. Phys.* **1960**, *31*, 1165.
[39] A. I. Kirkland, D. A. Jefferson, D. G. Duff, P. P. Edwards, I. Gameson, B. F. G. Johnson, D. J. Smith, *Proc.: Math., Phys. Eng. Sci.* **1993**, *440*, 589.
[40] V. Germain, J. Li, D. Ingert, Z. L. Wang, M. P. Pileni, *J. Phys. Chem. B* **2003**, *107*, 8717.
[41] J. Gal, *Chirality* **2011**, *23*, 647.
[42] W. Ma, L. Xu, A. F. de Moura, X. Wu, H. Kuang, C. Xu, N. A. Kotov, *Chem. Rev.* **2017**, *117*, 8041.
[43] D. S. Sholl, A. Asthagiri, T. D. Power, *J. Phys. Chem. B* **2001**, *105*, 4771.
[44] A. Kühnle, T. R. Linderoth, B. Hammer, F. Besenbacher, *Nature* **2002**, *415*, 891.
[45] J. Morales-Vidal, N. López, M. A. Ortuño, *J. Phys. Chem. C* **2019**, *123*, 13758.
[46] E. Herrero, L. J. Buller, H. D. Abruña, *Chem. Rev.* **2001**, *101*, 1897.
[47] T. Van Cleve, E. Gibara, S. Linic, *ChemCatChem* **2016**, *8*, 256.
[48] H. Bort, K. Jüttner, W. J. Lorenz, E. Schmidt, *J. Electroanal. Chem. Interfacial Electrochem.* **1978**, *90*, 413.
[49] A. Martins, V. Ferreira, A. Queirós, I. Aroso, F. Silva, J. Feliu, *Electrochem. Commun.* **2003**, *5*, 741.
[50] M. Pasta, F. L. Mantia, Y. Cui, *Electrochim. Acta* **2010**, *55*, 5561.
[51] H. Quan, S.-U. Park, J. Park, *Electrochim. Acta* **2010**, *55*, 2232.
[52] M. Tominaga, T. Shimazoe, M. Nagashima, H. Kusuda, A. Kubo, Y. Kuwahara, I. Taniguchi, *J. Electroanal. Chem.* **2006**, *590*, 37.